POLITECNICO DI TORINO
Repository ISTITUZIONALE

Strengthening strategies for an Al alloy processed by in-situ alloying during laser powder bed fusion

Original
Strengthening strategies for an Al alloy processed by in-situ alloying during laser powder bed fusion / Bosio, F.; Fino, P.; Manfredi, D.; Lombardi, M.. - In: MATERIALS & DESIGN. - ISSN 1873-4197. - ELETTRONICO. - 212:(2021), p. 110247. [10.1016/j.matdes.2021.110247]

Availability:
This version is available at: 11583/2974829 since: 2023-01-20T14:09:07Z

Publisher:
Elsevier

Published
DOI:10.1016/j.matdes.2021.110247

Terms of use:

This article is made available under terms and conditions as specified in the corresponding bibliographic description in the repository

Publisher copyright

(Article begins on next page)

07 May 2026

Materials & Design 212 (2021) 110247

Contents lists available at ScienceDirect

Materials & Design

journal homepage: www.elsevier.com/locate/matdes

Strengthening strategies for an Al alloy processed by in-situ alloying during laser powder bed fusion

Federico Bosio *,[1], Paolo Fino, Diego Manfredi, Mariangela Lombardi

Department of Applied Science and Technology, Politecnico di Torino, Corso Duca degli Abruzzi 24, 10129 Turin, Italy

HIGHLIGHTS

- AlSi10Mg + 4Cu alloy is succesfully processed by laser powder bed fusion in-situ alloying.
- Solid solution and precipitation strenghenting mechanisms are exploited for improving AlSi10Mg mechanical properties.
- Cu addition increased AlSi10Mg hardness and yield strength of 8.8% and 35.6%, respectively.
- Direct aging strategy is pursued to foster the alloy precipitation potential after rapid cooling.
- The maximum hardness response is attained after 1 h at 175 °C.

GRAPHICAL ABSTRACT

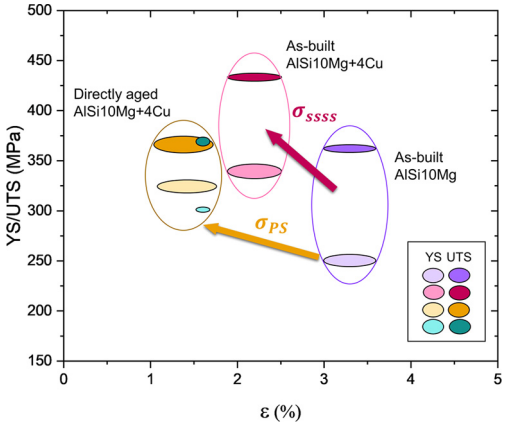

ARTICLE INFO

Article history:
Received 13 September 2021
Revised 29 October 2021
Accepted 9 November 2021
Available online 11 November 2021

Keywords:
Alloy development
In-situ alloying
Strengthening strategies
Super-saturated solid solution
Direct aging
Precipitation strengthening

ABSTRACT

In this work, a high strength Al alloy was successfully processed via *in-situ* alloying of AlSi10Mg and Cu elemental powders during Laser Powder Bed Fusion. To get superior strength, 4 wt% of Cu was added to AlSi10Mg composition to benefit from the additional solid solution and precipitation strengthening mechanisms induced by Cu atoms. Microstructure, chemical composition, hardness, and tensile properties of as-built samples were firstly determined. The microstructure showed a dual eutectic formed by Si precipitates intermixed with θ-Al_2Cu phase. The average Cu concentration was 3.96 ± 0.26 wt% in line with the theoretical one. Hardness and yield strength of AlSi10Mg + 4Cu alloy showed an increase of respectively 8.8 % and 35.6 % compared to the as-built AlSi10Mg, owing to the highly super-saturated solid solution of Si and Cu atoms upon rapid solidification. After that, a direct aging heat-treatment strategy was pursued to fully exploit the potential alloy precipitation by heating as-built samples at temperatures between 160 and 190 °C. A maximum hardness response was achieved after 1 h at 175 °C. The high hardening was primarily attributed to a mix of $\theta''/\theta' + \theta$-$Al_2Cu$ and Si phases coupled with a still high solid solution content. Nevertheless, direct aging slightly decreased the alloy ductility due to the prominent precipitation of brittle Si particles during aging and the presence of Cu inhomogeneities formed after *in-situ* alloying.

© 2021 The Author(s). Published by Elsevier Ltd. This is an open access article under the CC BY license (http://creativecommons.org/licenses/by/4.0/).

* Corresponding author.
E-mail addresses: federico.bosio@polito.it, federico.bosio@tii.ae (F. Bosio).
[1] Present address: Advanced Materials Research Centre, Technology Innovation Institute, Abu Dhabi, United Arab Emirates.

https://doi.org/10.1016/j.matdes.2021.110247
0264-1275/© 2021 The Author(s). Published by Elsevier Ltd.
This is an open access article under the CC BY license (http://creativecommons.org/licenses/by/4.0/).

1. Introduction

Laser Powder Bed Fusion (LPBF) paved the way for developing novel alloy compositions with peculiar characteristics that cannot be achieved with conventional manufacturing processes [1]. Although there has been an increased demand for new alloys compatible with LPBF, the material palette available in the marketplace is still quite limited [2]. Developing new alloys for LPBF requires, indeed, high economic resources due to the need for customized pre-alloyed powders [3]. In this regard, the *in-situ* alloying of elemental powder blends represents a low-cost method to explore new materials, providing a high degree of flexibility in material design and processing operations [1]. The alloy chemical composition is first designed. Afterward, the elemental powders are mixed within rotating jars and then *in-situ* alloyed on the powder bed exploiting the laser beam energy [4]. At this point, physical phenomena such as thermocapillary effect and recoil pressure induce a turbulent melt flow within the molten pool that helps to locally mix the constitutive alloy elements [5,6]. Thus, the local heat flux generated by the fusion of adjacent scan tracks induces a further diffusion of constitutive elements leading to the alloy consolidation [7].

The *in-situ* alloying has been widely investigated to modify existing high-strength Al alloys for improving their LPBF processability [8,9] or exploring novel Al compositions [7,10–12]. For instance, Montero Sistiaga et al. added 4 wt% of Si to a 7075 Al alloy to prevent liquation cracking [8]. The effect of Si on 7075 alloy was twofold. On the one hand, it reduced the alloy solidification range by lowering the alloy melting point. On the other hand, it acted as a grain refiner, promoting ultrafine-grained regions at melt pool overlapping areas. Similarly, Casati et al. successfully processed an Al-Zn-Si-Mg-Cu alloy by blending Al-Si-Mg and Al-Zn-Mg-Cu powders without hot cracks after rapid solidification [9]. However, despite its flexibility, the *in-situ* alloying often resulted in fluctuations of the chemical composition due to different melting points and thermal properties of the constitutive elements [7,10]. In this regard, Wang et al. used LPBF to *in-situ* manufacture Al-*x*Cu samples starting from Al-4.5Cu and Cu powder blends [7]. X-Ray Diffraction (XRD) analyses revealed that the reflections related to the pure Cu were no longer visible after *in-situ* alloying. Nevertheless, un-melted Cu particles were still detected in as-built Al-6Cu and Al-40Cu samples after imaging investigations. The chemical composition around those particles was rather inhomogeneous, resulting in a microstructure enriched of Cu. Notwithstanding this, the Authors supposed that the majority of Cu atoms were partly retained in the Al matrix and partly precipitated as Al_2Cu phase upon rapid solidification implying the possibility to exploit both solid solution and precipitation strengthening mechanisms.

In fact, it is known that the alloy lattice is locally distorted by the presence of solute atoms that hinder the dislocations gliding, thus strengthening the alloy. In this context, former studies reported an increased solid solubility limit of Cu in rapidly solidified Al alloys [13], suggesting the formation of a high supersaturated solid solution (SSSS) after the *in-situ* alloying when the Cu addition is lower than its typical solid solubility limit in Al (i.e., 5.65 wt% [14]). On the other hand, according to the general metallurgical principle of age-hardening for Al alloys [15], the maximum strengthening can be reached when gliding dislocations pass through precipitates with a fully coherent lattice with *fcc*-Al, i.e., when GP zones and the pioneers metastable phases coexist. For this reason, to trigger the precipitation of strengthening phases containing Cu from the SSSS, *in-situ* alloyed materials can be strengthened through direct ageing heat-treatments without pre-solutioning heat-treatments [16,17]. Unlike the well-known direct aging behavior of Al-Si-Mg alloys [18–21], to the best of our knowledge, the state-of-art on the aging response of Al-Si-Mg-Cu alloys processed by LPBF is limited to the work of Roudnická et al. [22]. In particular, the Authors have recently investigated the age-hardening response of an AlSi9Cu3 alloy processed by LPBF. After directly aging the alloy in the temperature range of 140–180 °C, an overall strengthening was recorded with a hardness and yield strength increment of 13–18% and 36%, respectively. In terms of metallurgical phases, a mix of θ' - Al_2Cu precipitates and Si platelets were revealed in the peak-aged condition, according to the precipitation sequence of the Al-Cu alloy system, i.e., GP (discs) $\rightarrow \theta''$ (discs) $\rightarrow \theta'$ (plates) $\rightarrow \theta$ (Al_2Cu).

For the purpose of exploiting both solid solution and precipitation strengthening mechanisms promoted by the Cu addition to improve the alloy strength, this paper presents the results of an AlSi10Mg alloy modified with 4 wt% of Cu powder, a typical amount giving hardening in 2*xxx* Al series [14]. Following recent research group's works [23,24], the *in-situ* alloying was adopted to mix and consolidate the alloy under the LPBF laser beam. In particular, this work aims at studying the direct aging behavior of the *in-situ* alloyed AlSi10Mg + 4Cu system. After a comprehensive characterization of the as-built material, the processed alloy underwent direct aging heat-treatments at various temperatures within the precipitation range for Al-Si alloys [25]. The aging response was then studied by tracking the hardness profile, and the significant direct aging conditions were deeply investigated in terms of microstructures, thermal behavior, and tensile properties.

2. Materials and methods

Gas-atomized powders of AlSi10Mg (EOS Gmbh) and high purity Cu (Sandvik Osprey LTD) were firstly mixed in a weight proportion of 96:4 using rotating jars and then *in-situ* alloyed during LPBF to synthesize AlSi10Mg + 4Cu alloy. The chemical composition of the starting powders and the calculated composition of AlSi10Mg + 4Cu is reported in Table 1.

After mixing of elemental powders, an EOSINT M270 Dual-mode LPBF system was used to produce bulk samples of AlSi10Mg + 4Cu. To this end, the process parameters, namely power, speed, layer thickness and hatching distance of 170 W, 1000 mm/s, 0.30 μm, and 0.14 mm, respectively, were used. These parameters were optimized in a previous work in order to maximize the productivity while maintaining a density higher than 99.16 % [23]. Two batches of samples were manufactured, namely cubes of 15 × 15 × 15 mm^3 for the as-built and direct aging characterization, and flat tensile specimens with a geometry according to ASTM E8/E8M-16a for the mechanical characterization. Reference samples of AlSi10Mg, either bulk or tensile ones, were built using the same LPBF system and its optimum process parameters [26].

The aging response of AlSi10Mg + 4Cu was directly assessed starting from the as-built condition (without previous solution heat-treatment), following the T5 temper protocol [16]. Direct aging temperatures were selected within the range for the precipitation heat-treatments of age-hardenable aluminum alloys, with a fixed interval of 15 °C, being 160 °C, 175 °C and 190 °C [25]. For all the temperatures, aging treatments were carried out at fixed times, i.e., 1, 2, 4, and 8 h. Heat-treatments were conducted in a heating oven (model BINDER FD56) with a temperature accuracy ΔT of ±1.5 °C. Aging behaviors were evaluated by performing Vickers micro-hardness tests (HV 0.5) by applying a static load of 0.5 Kg and a dwell time of 10 s using a HNVS-1000DX hardness tester. Five indentations were considered on each sample according to the ASTM E384-17 standard.

Table 1
The chemical composition of the used powders (wt.%).

Alloy	Si	Fe	Cu	Mn	Mg	Ti	O	Al
AlSi10Mg	9–11	≤ 0.55	≤ 0.05	≤ 0.45	0.2–0.45	≤ 0.15	–	Bal.
HCP Cu	–	–	≥ 99.96	–	–	–	≤ 0.04	–
AlSi10Mg + 4Cu[†]	8.6–10.6	≤ 0.55	4	≤ 0.45	0.19–0.43	≤ 0.15	≤ 0.04	Bal.

[†] the composition of AlSi10Mg + 4Cu mixed powder is calculated.

The microstructural and phase assessment of as-built and directly aged samples was performed by coupling XRD, Differential Scanning Calorimeter (DSC), and Field Emission Scanning Electron Microscope (FESEM) techniques.

The phase identification was performed by XRD on the XZ cross-sections of as-built and directly aged samples using a X-Pert Philips PW3040 diffractometer in Bragg Brentano configuration. A first batch of XRD patterns was obtained in the 2θ range from 20 to 100° at steps of 0.013°, and step duration of 25 s. After that, a second round of XRD analyses was performed to deeply investigated some peaks, between 42° and 48°, using a finer step size (0.0033°) and an implemented duration time (60 s). Apart from the peaks/phases identification, XRD data were also used to calculate the *fcc*-Al lattice parameter according to cos θ cot θ method [24].

A Setaram TGA 92 16.18/DSC was employed to investigate the precipitation sequence of strengthening phases. DSC scans were carried out in the temperature range from 50 to 450 °C with a heating rate of 10 °C/min. To equilibrate the heat flux, an initial isothermal step of 15 min at 50 °C was performed before DSC scans. Empty Al_2O_3 crucible was used as a reference. The same heating program was used for as-built and directly aged specimens.

Samples for microstructure investigation were grinded and polished by standard metallographic technique up to 1 μm; final finishing was obtained using a 0.04 μm colloidal silica. The chemical etching was then conducted in a diluted Keller solution (20% Keller reagents, 80% H_2O) for 10 s. Microstructural phases were observed by a Zeiss SupraTM 40 FESEM microscope coupled with an Energy Dispersive X-ray (EDX) detector for chemical composition mapping. For an estimation of the Cu content after the *in-situ* alloying, four EDX maps were conducted on XZ samples cross-sections with a magnification of 310X. Each map scanned an area of 400 × 400 μm^2.

Finally, as-built and directly aged tensile specimens were tested by using a Zwick Z100 tensile machine applying a strain rate of 8×10^{-3} s^{-1}. All tests were carried out at room temperature. To ensure a representative tensile behaviour, 3 samples for each condition were considered. The fracture surfaces of tested samples were then investigated by FESEM.

3. Results

3.1. As-built AlSi10Mg + 4Cu via in-situ alloying

The LPBF AlSi10Mg + 4Cu samples revealed a densification level of 98.97 ± 0.21 % measured by image analysis, confirming that near fully dense materials were successfully produced adopting the method previously proposed by the Authors [23].

Fig. 1a shows a low magnification macrostructure of the as-built AlSi10Mg + 4Cu alloy across its longitudinal plane. The alloy displays the typical morphological texture observed for other LPBF*ed* Al alloys [26–28]. A 'fish scale' pattern formed by piled-up melt pools was revealed. Besides, it was possible to observe the presence of brighter regions located near the overlapping areas between nearby fusion lines, corresponding to Cu segregations (Fig. 1b).

A representative FESEM micrograph of the as-built AlSi10Mg + 4Cu alloy is reported in Fig. 1c. The microstructure reveals the extremely fine cellular/columnar dendritic architecture induced by the severe constitutional undercooling stored during the rapid cooling from the melt. Dendrites epitaxially grew at the melt pool boundary and are oriented towards the melt pool center, opposite to the heat flux extraction [29].

Moving from the core to the boundary of a melt pool, a variation of the microstructural features can be noticed (Fig. 1d-f) [30]. In the melt pool core (MP core), indeed, the solidification mode was mainly cellular-dendritic, resulting in a continuous eutectic architecture with fine cells of size 0.8 ± 0.4 μm (Fig. 1d). Going towards the melt pool boundary a coarser texture was observed, labelled as 'MP coarse' zone. Here, the solidification mode was cellular/columnar dendritic, as can be observed in Fig. 1e. The eutectic pattern was still discernible, although network interruptions and dendrite sided branches were observed to a large extent. Lastly, in the Heat Affected Zone (HAZ)Fig. 1f), the eutectic architecture was broken into several particles due to the laser remelting occurred during manufacturing.

As also reported in our previous work [24], the eutectic network of AlSi10Mg + 4Cu was constituted by an intermixing of eutectic Si particles and θ-Al_2Cu phase. This was corroborated by the XRD pattern reported in Fig. 1g of this study. The XRD reflections, indeed, revealed the presence of fcc-Al, diamond cubic Si and tetragonal Al_2Cu phase (i.e., θ phase).

Lastly, the thermal behavior of the as-built AlSi10Mg + 4Cu alloy is depicted in Fig. 1h. Two distinct exothermic signals are identified. The temperatures of these peaks are in agreement with those recorded for an LPBF*ed* AlSi10Mg alloy in a recent research [31]. The first most intense peak is centered at 236 °C. The exothermic nature of the peak indicated that some precipitation reactions occurred between 185 °C (i.e., the peak onset temperature) and 275 °C. As evidenced for the as-built AlSi10Mg alloy [31], this signal accounted for the Si diffusion and its precipitation from the SSSS. However, this exothermic peak might also account for the formation of other precipitates. In fact, transition intermetallic phases such as θ'-Al_2Cu [32], β'' -Mg_2Si [33–35], and S'-Al_2CuMg [36] form within a similar temperature range. Therefore, it might be probable that their corresponding precipitation signals contributed to the intensity of the first exothermic peak of Fig. 1h. By increasing the temperature, a less intense signal centred at around 318 °C is encountered on the thermogram. In this case, the peak is related to the precipitation of Mg_2Si and phases containing impurity elements [31].

3.2. Direct aging of AlSi10Mg + 4Cu

3.2.1. Aging response

The aging behaviors of the AlSi10Mg + 4Cu alloy are depicted in Fig. 2. Before direct aging heat-treatments, the as-built samples exhibited an average hardness of 142.3 ± 5.0 HV. The as-built micro-hardness value of AlSi10Mg + 4Cu was higher than the AlSi10Mg counterpart (i.e., 130.8 ± 3.1 HV), showing a hardness increment of 11.5 HV (i.e., 8.8 %). On aging, micro-hardness followed different trends according to the used aging temperature.

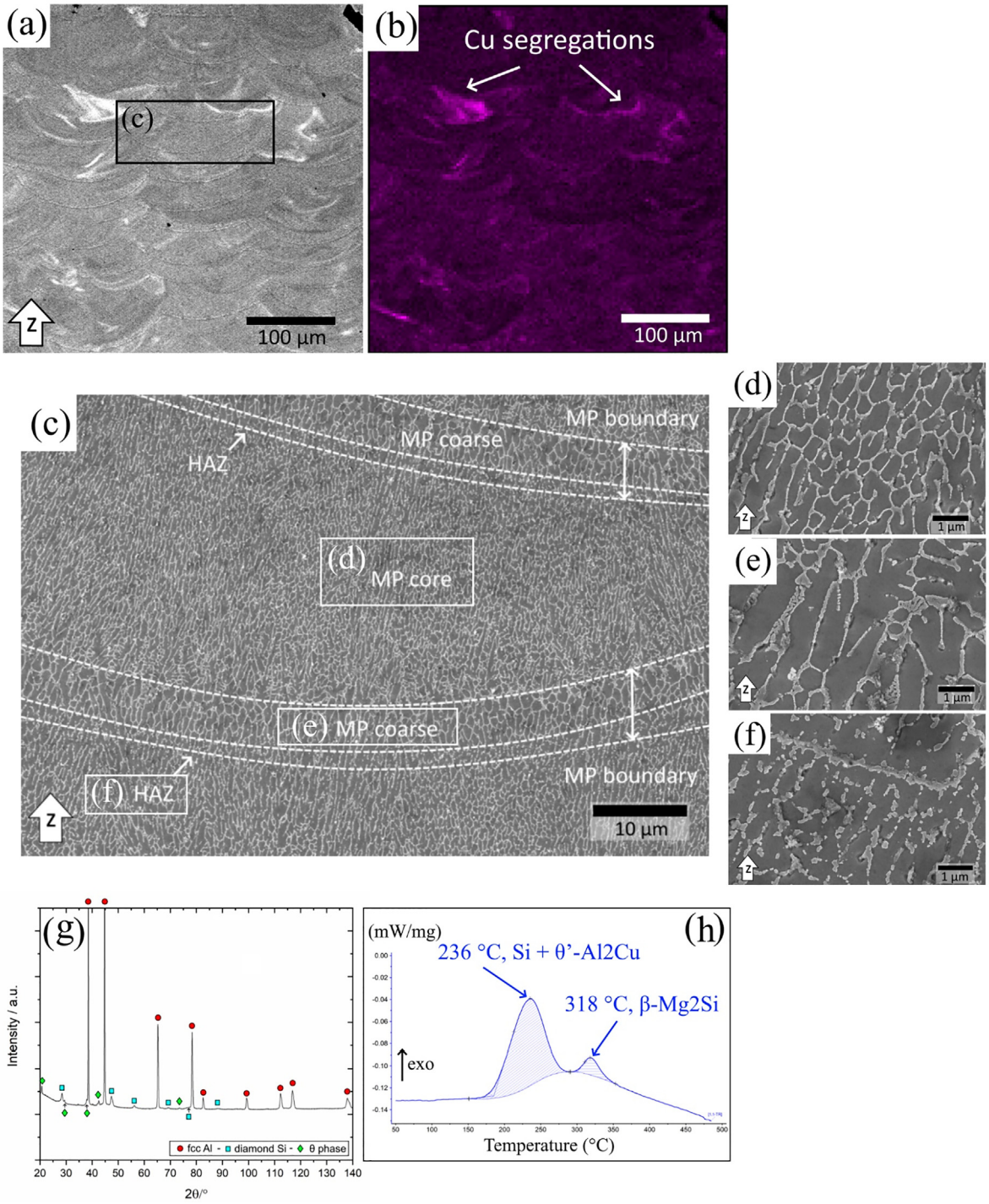

Fig. 1. Schematic overview of the characterization performed on the as-built AlSi10Mg + 4Cu alloy obtained via in-situ alloying: (a) a micrograph and (b) the Cu distribution map along the longitudinal cross-section of a bulk sample; (c) a FESEM micrograph showing the different regions of a melt pool and the corresponding insets related to: (d) MP core, (e) MP coarse, and (f) HAZ; (g) the XRD pattern and (h) the DSC thermogram.

When aging was conducted at 190 °C, the aging curve went through a hardness peak after an elapsed time of 2 h. Then, a relevant hardness drop was detected, suggesting a possible over-aging. By decreasing the aging temperature to 175 °C, a hardness peak was identified upon 1 h. Afterward, hardness slightly decreased at higher aging times while remaining well above its as-built value. As far as the aging behavior at 160 °C is concerned, hardness increased steadily up to 4 h. Then, beyond this point, the HV values reached a plateau.

Table 2 summarizes the maximum hardness (HV_{max}) obtained for each condition, along with the time to peak-age and the relative hardness increment (ΔHV_{max}) values with respect to the hardness

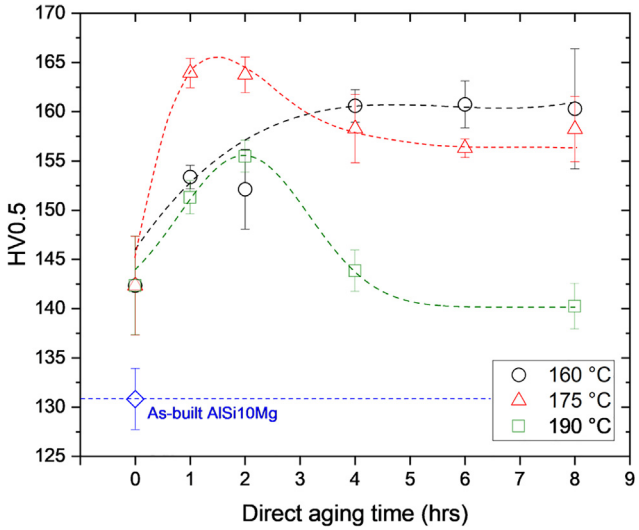

Fig. 2. Aging curves of AlSi10Mg + 4Cu alloy at different aging temperatures and times.

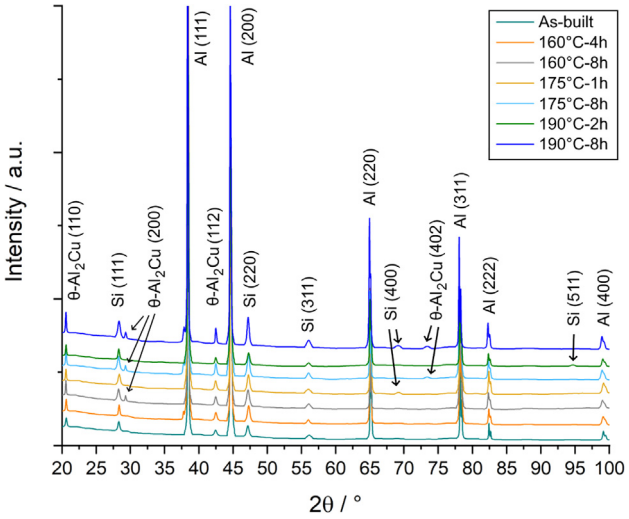

Fig. 3. XRD patterns of as-built and directly aged AlSi10Mg + 4Cu samples.

of the as-built AlSi10Mg + 4Cu material. As can be noticed, a limited hardening response was achieved at 190 °C, whereas higher hardness was attained at the lower temperatures, i.e., 160 °C and 175 °C.

3.2.2. Phase identification

Figs. 3 and 4 report XRD patterns of samples characterized by the maximum hardness after direct aging heat-treatments (Table 2). As-built and aged samples at 8 h for each aging temperature were also reported to detect the constitutional phase evolution during direct aging treatments. As for the as-built alloy, XRD patterns revealed reflections due to the presence of *fcc* Al, diamond cubic Si, and tetragonal θ-Al_2Cu phases. It can be noticed that the position of Al peaks gradually shifted to lower angles by increasing the aging temperature and time, as clearly observable for the Al (200) peak positions reported in Fig. 4a. This could indicate a progressive depletion of the SSSS formed by Si and Cu atoms during the direct aging heat-treatment [37].

As denoted by the Si (200) peaks of Fig. 4b, Si reflections became sharper and more intense with the increasing aging temperature and time. This corroborates the idea that, during aging, Si moved out of the SSSS to precipitate at the Al cell boundaries [37,38].

A similar trend was found for the θ-Al_2Cu phase. Indeed, at a constant aging temperature, higher peak intensities were detected at the longer aging time, namely after 8 h, as observed in θ-Al_2Cu (112) reflections of Fig. 4c. Moreover, it must be noted that minor peaks referring to the θ-Al_2Cu phase, i.e. (200), (402) and (310) reflections, appeared after 8 h of heat-treatment (see Fig. 3 and Fig. 4b).

The lattice parameter values for the *fcc* Al of studied specimens were plotted against the direct aging times in Fig. 5. Results revealed a general broadening of the Al lattice parameter on the increasing aging time. Based on the linear fitting, it could be inferred that within the investigated time interval and temperatures, the higher the aging time, the larger is the Al lattice parameter. Lastly, the slope of the linear trends ranked in the sequence 160 < 175 < 190 °C, suggesting an influence of the aging temperature on the increment of the Al lattice parameter.

3.2.3. Thermal behavior

As already stated, the as-built sample showed a thermogram with two prominent exothermic peaks in correspondence with the precipitation of Si and Cu precipitates in the former and $MgSi_2$ in the latter (Fig. 1h). After aging at 160 °C (Fig. 6a), the first exothermic signal slightly shifted at a higher temperature compared to the as-built condition. In this regard, it must also be pointed out that the peak intensity gradually decreased when increasing the aging time. Apart this, DSC scans did not show any other significant differences in the investigated temperature interval. Similarly, aging the alloy at 175 °C for 1 h reduced the first exothermic peak enthalpy from 22.5 to 12.9 J/g (Fig. 6b). After a direct aging time of 8 h at the same temperature, this peak completely disappeared, suggesting that Si and $\theta''/\theta'/\theta$-phase precipitations already occurred during the direct aging heat-treatment. By further increasing the aging temperature to 190 °C (Fig. 6c), the first exothermic signal was still identifiable upon 2 h, although the released enthalpy was relatively low (2.2 J/g), and then entirely disappeared after 8 h of direct aging treatment.

3.2.4. Microstructure

Fig. 7 reports the representative FESEM micrographs of AlSi10Mg + 4Cu alloy after direct aging heat-treatments. Upon aging at 160 °C (Fig. 7a,b), the microstructure did not show significant variations compared to the as-built ones (Fig. 1c), still show-

Table 2
Temperature and time to the maximum hardness (HV_{max}), mean HV_{max} and its standard deviations (St. Dev.), and the relative hardness increment (ΔHV_{max}) as compared to the as-built AlSi10Mg + 4Cu hardness value. The hardness increase calculated with respect to the as-built AlSi10Mg hardness value is also reported.

Aging temperature (°C)	Time to HV_{max} (h)	HV_{max}		$\Delta HV_{max\text{-}AlSi10Mg4Cu}$	$\Delta HV_{max\text{-}AlSi10Mg}$ (%)
		Mean	St. Dev.		
160	4	160.6	1.6	18.3	22.8 %
175	1	163.9	1.5	21.6	25.3 %
190	2	155.5	1.6	13.1	18.9 %

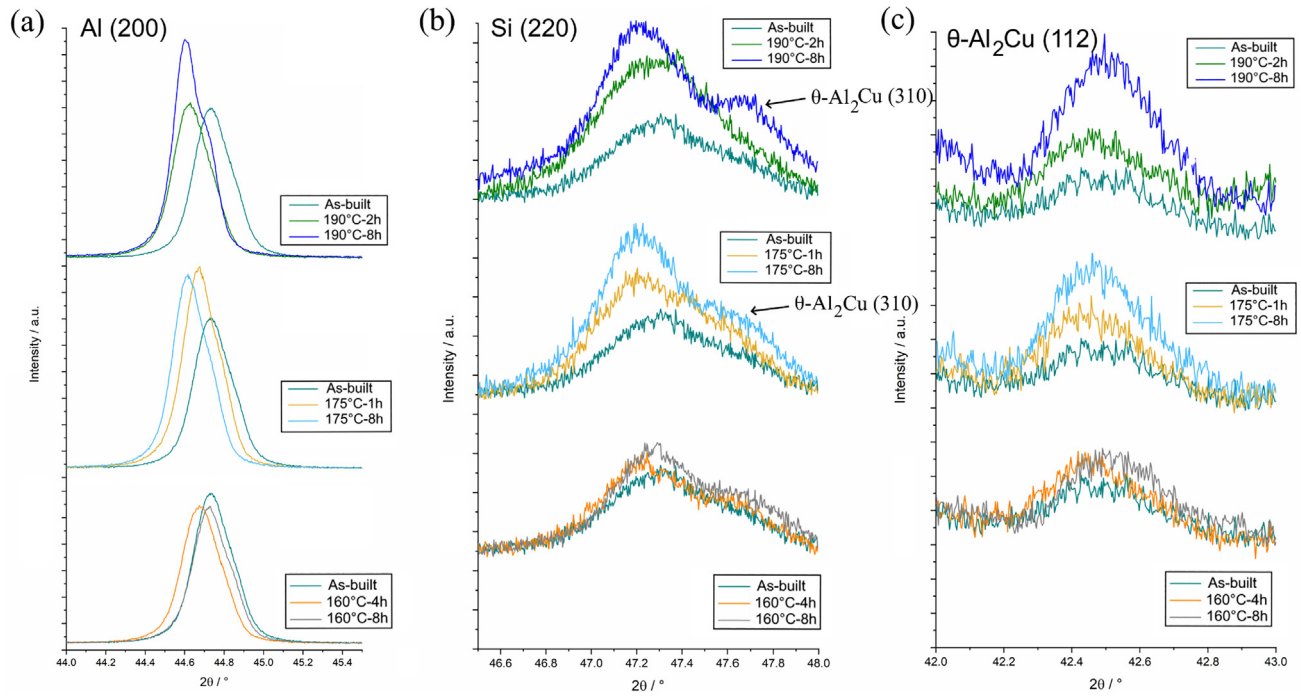

Fig. 4. Detail of (a) Al (200), (b) Si (200) and (c) (112) θ-Al_2Cu reflections.

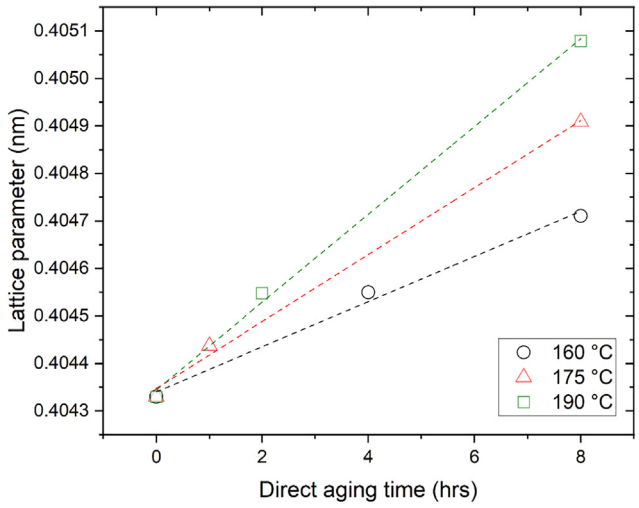

Fig. 5. Relationships between Al lattice parameter and the direct aging temperature.

ing a fibrous eutectic architecture. By raising the aging temperature to 175 °C (Fig. 7c,d), the eutectic network was still identifiable. However, in Fig. 7d, it was noticed the presence of tiny particles within the α-Al cells, which likely precipitated out of the SSSS during the aging heat-treatment [18,20]. This was clearly observed after aging at 190 °C. In fact, the micrographs of Fig. 7e,f were strewn with very fine precipitates randomly distributed on sample surfaces. Here, the eutectic network was rather discontinuous likely due to the eutectic constitutive elements diffusion through aging heat-treatment and the subsequent network spheroidization [34,39].

3.3. Tensile characterization and surface fracture analysis

Results of tensile tests conducted on the as-built and peak-aged specimens of AlSi10Mg + 4Cu are summarized in Fig. 8 and Table A 1. The tensile properties of an as-built AlSi10Mg alloy were reported for comparison. As can be noticed in Fig. 8, the as-built AlSi10Mg + 4Cu alloy shows higher yield strength (YS) and ultimate tensile strength (UTS) values compared to the base AlSi10Mg alloy. In fact, by mixing 4 wt% of Cu with AlSi10Mg, an increment of YS and UTS of respectively 35.6 % and 19 % was achieved. However, the strengthening effect of Cu induced a reduction of the elongation at break from 3.3 % to 2.2 %. As far as the peak-aged specimens of AlSi10Mg + 4Cu are concerned, their tensile strengths were still higher than that of as-built AlSi10Mg. In Fig. 8, the main strengthening mechanisms that contributed to AlSi10Mg + 4Cu strength were also reported. A comprehensive discussion is provided in Section 4.

Fracture surfaces of the as-built and directly aged tensile AlSi10Mg + 4Cu samples were investigated to determine the prevailing failure mechanism. Before analyzing the results in more detail, it was observed that directly aged fracture surfaces resembled those of the as-built condition. Therefore, no significant differences were visible among the investigated tensile specimens. The representative fracture surface topography of a tensile specimen heat-treated at 175 °C for 1 h was reported as an example in Fig. 9a. A detailed examination of Fig. 9a revealed the presence of irregular and elongated cavities (pointed by yellow arrows), likely originated by lack-of-fusion regions between adjacent tracks or layers. Apart from these lack-of-fusion areas, fracture surfaces were dotted with several holes (pointed by red arrows) showing nearly spherical shapes. Fig. 9b provides a close-view of a spherical cavity, which exhibited a diameter of roughly 112 μm. A deep investigation inside the cavity evidenced the occurrence of brittle particles at the bottom, presumably oxides, and, occasionally, the presence of un-melted particles. By further increasing the magnification, it was possible to appreciate the nature of the failure micromechanism. As can be observed in Fig. 9c, a combination of brittle and ductile fractures was locally found. In fact, a brittle area with a facet-like appearance likely originated from a cleavage fracture coexisted with a more ductile area, which showed very fine dimples with a size lower than 1 μm (Fig. 9d). A close-view of the duc-

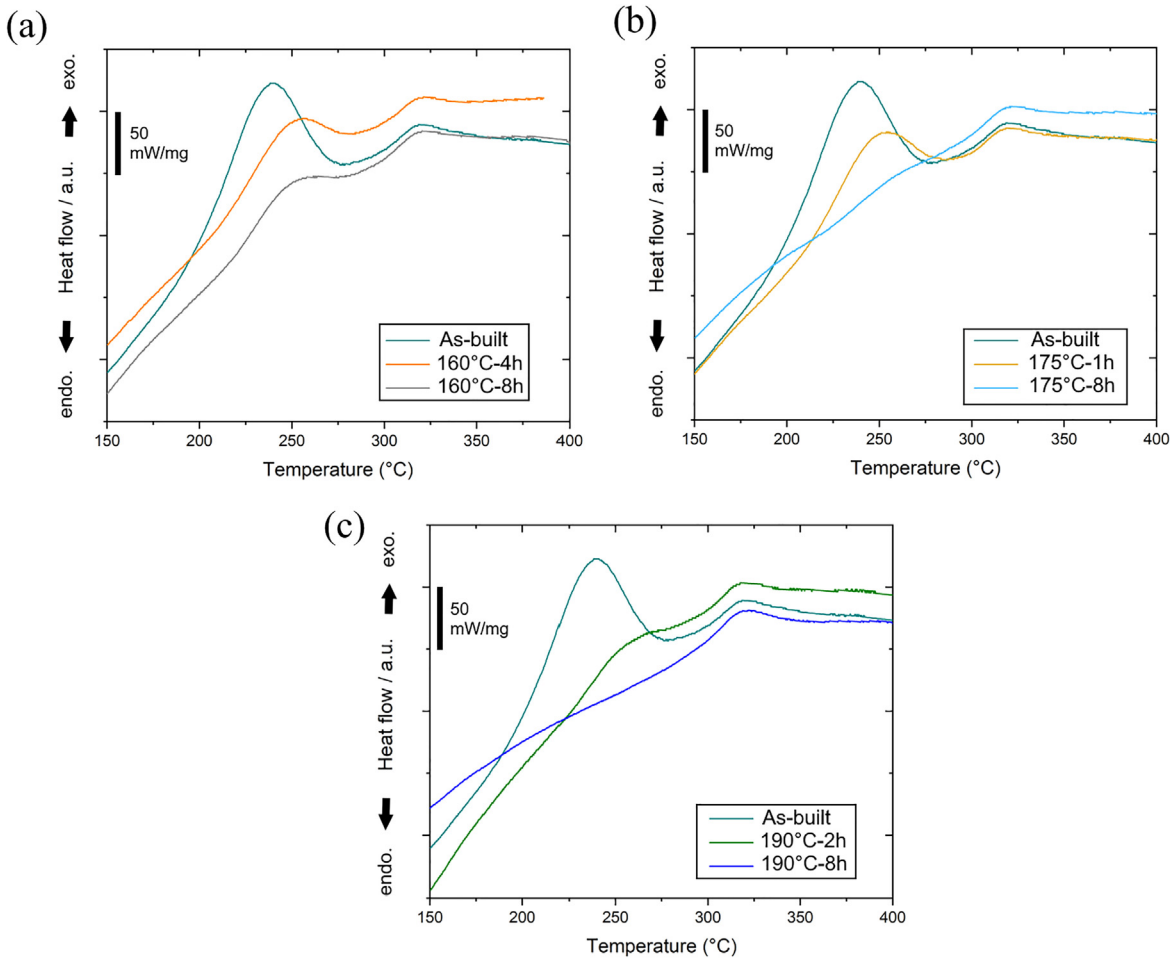

Fig. 6. Results of DSC scans performed on as-built and heat treated samples at (a) 160 °C, (b) 175 °C and (c) 190 °C.

tile region revealed nanometric precipitates within the dimple cells, as shown in Fig. 9e.

4. Discussion

LPBF has shown to be a unique additive manufacturing technique that develops very high heating and cooling rates (10^3-10^8 K/s) during the printing process [40]. These local conditions typically lead to the formation of extremely fine microstructures, metastable phases, and enhanced solid solubility, making possible to tailor novel alloy compositions for LPBF [41]. In this regard, Polmear et al. reported the solid solubility extension of the leading Al solute elements in samples produced by rapid cooling techniques [13,14]. For instance, they showed how the solubility limit of Cu in Al can be pushed to 42 wt% in metastable conditions instead of the 5.65 wt% reached at the equilibrium after a slow cooling process [13].

Hence, in this work, 4 wt% of Cu powder was added to a commercial AlSi10Mg alloy to achieve a high super-saturated solid solution level via *in-situ* alloying. Then, the potential precipitation of θ-Al_2Cu phase and its transition phases in AlSi10Mg + 4Cu samples was fully exploited by direct aging the alloy to increase the alloy hardness and strength.

The hardness and tensile properties of as-built and directly aged AlSi10Mg + 4Cu samples were superior to the as-built AlSi10Mg ones (Fig. 2 and Fig. 8). The improved strength of the as-built AlSi10Mg + 4Cu can be entirely ascribed to the addition of Cu, being both alloys processed by using the same LPBF machine and their optimum process parameters [23,24,31].

In this regard, it is thought that the presence of Cu had a beneficial effect on the alloy strengthening mechanisms. In general, previous works in literature expressed the overall strength of Al alloys by LPBF as the superimposition of the following contributing mechanisms [22,42]:

$$\sigma_{YS} = \sigma_{GBS} + \sigma_{SSSS} + \sigma_{PS} \tag{4.2}$$

where σ_{YS} is the yield strength of the alloy, σ_{GBS} the contribution of the grain boundary strengthening, σ_{SSSS} the contribution associated with the super-saturated solid solution, and σ_{PS} the contribution from precipitation strengthening.

Upon LPBF consolidation, the *in-situ* alloying of AlSi10Mg + 4Cu powder was achieved to a large extent, as demonstrated by the Cu diffusion in the as-built bulk sample (Fig. 1b). EDX results revealed, indeed, a Cu concentration of 3.96 ± 0.26 wt%, which was in good agreement with the theoretical Cu concentration in our alloy, i.e., 4 wt% (Table 2). However, the representative Cu distribution map of Fig. 1b indicated the presence of Cu segregations, mainly located in correspondence of the overlapping regions between adjacent melt pools. As suggested by Wang et al. [7], the origin of the observed Cu distribution can be explained considering the thermal effect produced by the fusion of subsequent scan tracks or layers during LPBF. When scan tracks/layers were scanned, the energy input was transferred to the previous laser tracks by conduction, and a remelting zone formed in the overlap area of adjacent single scans. Therefore, the diffusion of Cu atoms located near overlap

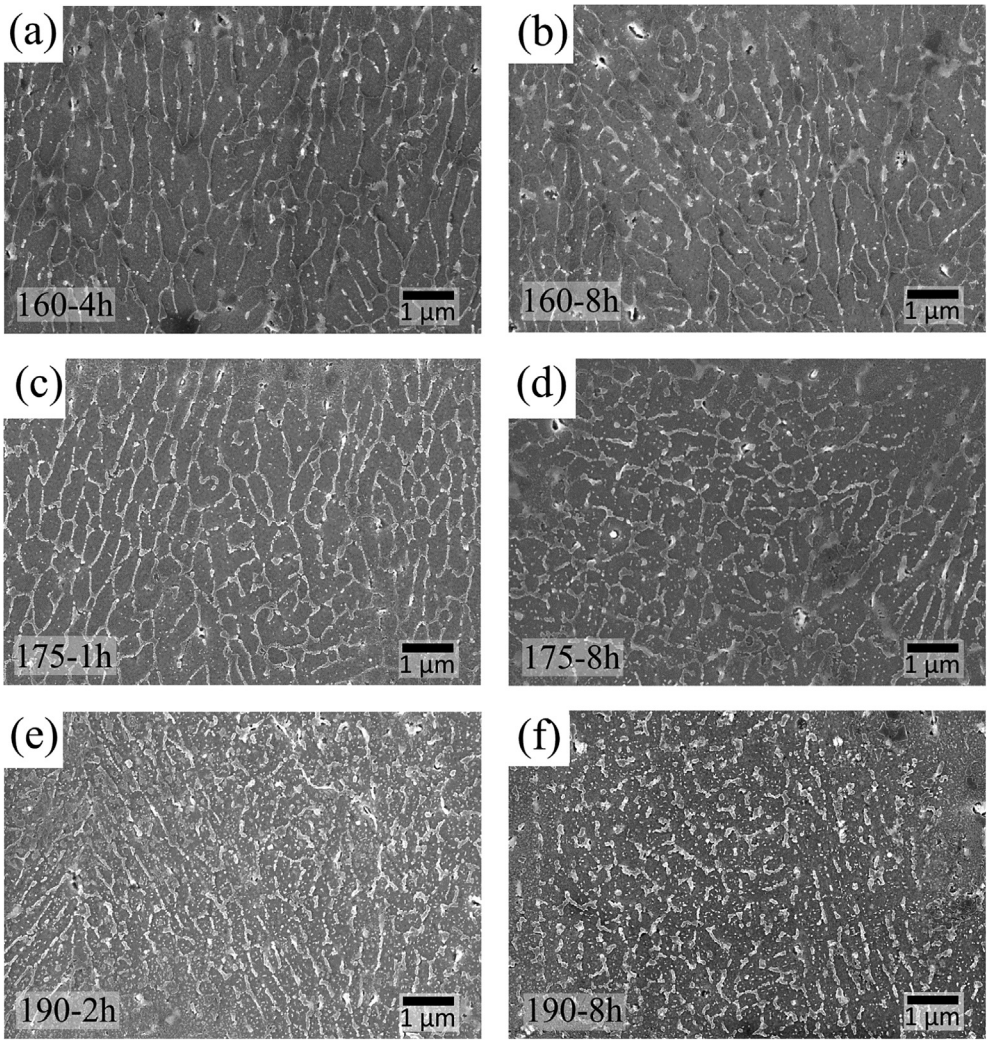

Fig. 7. FESEM microstructures in the MP core of AlSi10Mg + 4Cu samples directly aged at their peak age condition and after 8 h for each aging temperature.

regions was triggered. Then, Cu locally diffused towards the overlapping areas following the preferential diffusional paths tracked by the local heat flux and forming, eventually, Cu segregations at the melt pool boundaries.

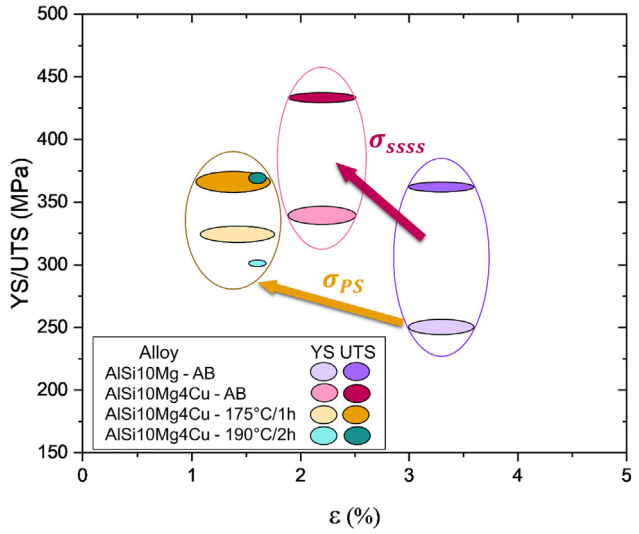

Fig. 8. Tensile test data for as-built and directly aged AlSi10Mg + 4Cu, in comparison with as-built AlSi10Mg.

Apart from areas enriched of Cu (Fig. 1b), the as-built AlSi10Mg + 4Cu microstructure observed at higher magnification revealed a fibrous eutectic architecture (Fig. 1d). In an Authors' previous work [24], it was reported that the eutectic structure was formed by Si precipitates intermixed with Cu-rich areas, surrounding very fine α-Al cells [24]. In this study, the FESEM micrographs reported in the Appendix section corroborate these characteristics (Fig. A 1). Due to the presence of θ reflections in XRD of Fig. 1g, it is plausible that eutectic Cu-rich areas, i.e., the brighter regions in Fig. A 1, were partly constituted by θ phase that suddenly precipitated out from SSSS because of the LPBF rapid cooling. However, as documented by previous studies of others research groups [27,30], a microstructural gradient was revealed moving from the MP core to the boundary (Fig. 1c-f). The cooling rate experienced by the melted alloy during solidification played a key role to determine the gradient and the fineness of said microstructure [43]. Due to the Gaussian profile of the employed laser, the melt temperature reached its maximum at the MP core, thus leading to a high thermal gradient G over the MP core region. In a similar way, the growth rate R, which corresponds to the displacement of the crystal solidification front in the time unit [43], met its peak at the fusion centreline, i.e., the MP core area. Therefore, a very high cooling rate ($G \times R$) occurred at the MP core, thus

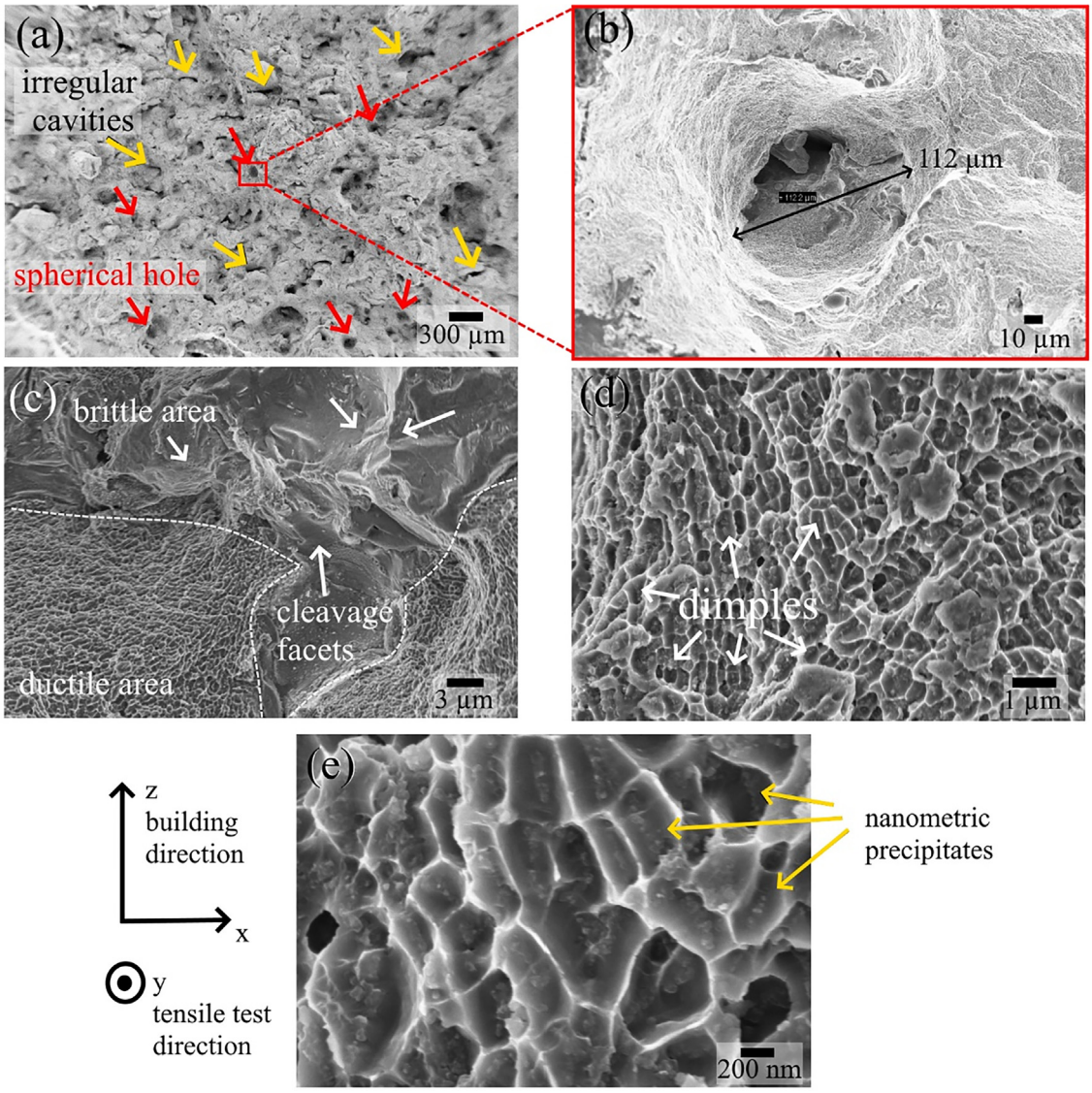

Fig. 9. (a-e) The fracture surface of an AlSi10Mg + 4Cu specimen directly aged for 1 h at 175 °C.

reducing the energy barrier for crystal nucleation and, consequently, promoting the formation of fine cells [27]. Eventually, moving from MP core to the boundary, the product $G \times R$ decreased, and eutectic cells became coarser as the melt experienced a slower solidification [44].

The mean size of α-Al cells in the melt pool core of AlSi10Mg + 4Cu samples was of the same order of magnitude as the as-built AlSi10Mg [24,31]. Furthermore, the EBSD maps corresponding to the XY plane of an as-built AlSi10Mg + 4Cu sample (Fig. A 2) showed no discrepancy of Al grain size after Cu addition with respect to the as-built AlSi10Mg [45]. To prove this, the average sizes of the equiaxed grains of both alloys were calculated using the equivalent circle diameter approximation. Results returned values of d_{AlSiMg} and $d_{AlSiMgCu}$ equal to7.56 and 7.34 µm, respectively. The σ_{GBS} contributions to the alloys yield strength were then calculated in accordance with the Hall-Petch equation [14], as follows:

$$\sigma_{GBS} = \sigma_0 + kd^{-1/2}$$

where σ_0 is 10 MPa [42], and the Hall-Petch coefficient k is 0.4 MPa/mm^2 [46]. Accordingly, we obtained $\sigma_{GBS/AlSi10Mg}$ of 14.6 MPa, and $\sigma_{GBS/AlSi10Mg4Cu}$ of 14.7 MPa. Therefore, it can be stated that the σ_{GBS} contributions did not justify the strength increment observed with the Cu addition in this work.

Among the various strengthening mechanisms, σ_{SSSS} mainly contributed to increasing the strength of as-built AlSi10Mg + 4Cu alloy. Under the assumption that the Si super-saturation content of AlSi10Mg + 4Cu was similar to that of the master AlSi10Mg alloy, i.e., 4 at.% [31], the Cu atoms in solid solution, i.e., 1 at. % [24], induced an extra-distortion of *fcc* α-Al lattice (Fig. 5), thus producing additional residual strains. Therefore, the dislocations gliding was effectively hindered by these solute-induced residual strains, and the strength of the alloy increased accordingly, with a reduction of ductility [47]. The σ_{SSSS} contributions to the alloys yield strength were estimated according to the model established by Myhr et al. [48] for Al-Mg-Si-Cu alloys:

$$\sigma_{SSSS} = \sum_j k_j c_j^{2/3}$$

where c_j is the concentration of j - solute element in solid solution, i.e., mainly Si, Cu, and Mg for Al-Si-Mg-Cu systems, and k_j is the corresponding power law coefficient of each solute species, as reported in Ref. [48]. The σ_{SSSS} calculations were conducted assuming that all

the Mg solutes were in SSSS after rapid cooling. By applying the model, we get a $\sigma_{SSSS/AlSi10Mg}$ and $\sigma_{SSSS/AlSi10Mg4Cu}$ of respectively 186.8 and 256.4 MPa corroborating our expectations. The difference of these values represents the additional SSSS strength induced by Cu addition, i.e., 70 MPa.Apart from solutes strengthening, dislocations slip was also pinned by disseminated θ-Al_2Cu precipitates detected by XRD in as-built AlSi10Mg + 4Cu samples (Fig. 1g), thus giving a further strengthening by precipitation (σ_{PS}). However, it must be highlighted that the specific contribution of the θ phase to the overall as-built strength was limited since θ is typically characterized by a body-centered crystal structure, which is incoherent with the *fcc*-Al lattice [15]. Indeed, it is well known that the higher strengthening contribution is achieved when gliding dislocations are forced to go through coherent precipitates [14]. In this work, we did not clearly detect coherent transitions phases [17], but the exothermic signals associated with θ'-Al_2Cu and β-Mg_2Si precipitations in Fig. 6 could point to the presence of their pioneer transition phases (GP/θ''/θ'-Al_2Cu and GP/β''/ β'- Mg_2Si) already in the as-built condition [35]. Furthermore, in the Authors' recent publication [24], it was calculated that Cu-modified AlSi10Mg samples have a higher eutectic fraction compared to the base AlSi10Mg (i.e., + 8 to 13%). In this scenario, the high volume of eutectic, which is constituted by Si intermixed with Al_2Cu precipitates [24], may have contributed consistently to the AlSi10Mg + 4Cu strength increment exploiting the Orowan mechanism [49].

Despite the presence of Si/Al_2Cu precipitates in the as-built condition, Marola et al. demonstrated that Si and Cu atoms were still largely trapped into the fcc-Al lattice owing to the severe constitutional undercooling induced by LPBF [24]. Therefore, this high grade of super-saturation provided a significant driving force for Si and Cu atoms to diffuse and nucleate metastable phases during direct aging heat-treatments [33].

In fact, by heating the alloy at the investigated aging temperatures, the precipitation process started with the diffusion of Si and Cu atoms within α-Al matrix [39]. Apart from the heat given by the furnace, diffusion of solutes was accelerated by the high concentration of vacancies induced by the fast cooling of LPBF, and, consequently, the nucleation of metastable phases occurred rapidly [33]. This was corroborated by the sudden reduction at short aging times of the released enthalpy associated with the precipitations of Si and θ' -Al_2Cu phase, as depicted in DSC scans of Fig. 6.

As the nucleation and growth of Si and Al_2Cu precipitates proceeded, the degree of super-saturation decreased accordingly, as proved by the increment of the Al lattice parameter with the direct aging time in Fig. 5. Therefore, as the aging time went by, the progressive diffusion of Si and Cu atoms from SSSS and the consequent nucleation and growth of Si/Al_2Cu precipitates, induced a relaxation of Al lattice. As can be noted by Fig. 5, the solutes diffusion rate was also found to be strictly related to the direct aging temperature [17]. The higher the aging temperature, the faster is the solutes diffusion from SSSS and then the nucleation of secondary phases containing Si and Cu.

The solutes diffusion dependence on the aging temperature can help to rationalize the different hardening responses reported in Fig. 2. The adoption of aging temperatures relying on the low range of the age temperature interval for Al-Si alloys [25], such as 160 °C, enabled a slow solutes diffusion and a gradual and delayed hardening. This was ascribed to the fact that, by keeping the aging temperature below the metastable solvus line for the formation of GP zones, i.e., in the range of 140–160 °C [19,25], the full precipitation sequence was exploited and, consequently, a delayed peak-age can be reached. For this reason, it is thought that the alloy heat-treated at 160 °C did not yet completely reached the peak-age condition within the investigated time interval. This can be primarily explained by the fact that XRD reflections of Fig. 4 did not show significant changes in the intensity of Si (200)/θ-Al_2Cu (112) peaks or shift to lower angles of Al (200) peak by increasing the direct aging time. In line with our assumption, the work of Roudnická et al. [22] showed that the peak-age condition for an LPBF*ed* AlSi9Cu3 alloy aged at 160 °C was reached at around 10 h, i.e., beyond the upper limit of our heat treatment time interval.

By increasing the aging temperature to 175 °C, a peak-age of 163.9 HV was achieved only after 1 h of aging time (Table 2). In this case, it is likely probable that Cu and Si atoms diffused rapidly from SSSS forming Si and a mix of $\theta''/\theta' + \theta$ -Al_2Cu precipitates. On the one hand, Si and θ-Al_2Cu precipitations were confirmed by the more intense Si (200) and θ -Al_2Cu (112) reflections recorded for samples AlSiMg10Mg + 4Cu heated at 175 °C/1h when compared to the as-built ones (Fig. 4). On the other hand, the lesser intense but still present exothermic peak of Si and θ' precipitations in the DSC scan measured for the sample aged at 175 °C/1h can give a clue for the presence of metastable θ''/θ' phases (Fig. 6b). Apart from the contribution of these precipitates to the overall hardness, it must be noted that, after 1 h at 175 °C, there still was a certain amount of solutes within the matrix, which brought a further strengthening by solid solution (see the lattice parameter value for 175 °C/1h in Fig. 5). Therefore, the proper balance between solid solution and precipitation strengthening mechanisms allowed to achieve the maximum hardness within a limited aging time (Table 2).

By further increasing the aging temperature to 190 °C, the solutes diffusion and nucleation was further speed-up. Under this condition, since the applied aging temperature relies on the high range of the aging temperature interval for Al-Si alloys [25], the formation of metastable phases θ''/θ' might have skipped or, whether they precipitated, quickly formed to a lower extent. In fact, the exothermic signal of Si + θ'-Al_2Cu was barely identifiable after just 2 h at 190 °C, thus pointing to an untimely formation of the stable θ -Al_2Cu phase (Fig. 6c). Furthermore, as can be deduced from the microstructure of Fig. 7e,f, Si and Cu solutes precipitated out from the eutectic breaking the fine network and forming the idiomorphic precipitates [27]. In this regard, considering the appearance of minor reflections of the Si and θ-Al_2Cu phases in the XRD results of samples aged at 190 °C (Fig. 3), it can be reasonable to conclude that these precipitates were mostly Si and θ-Al_2Cu particles. All these considerations rationalize the lower strengthening reached by aging AlSi10Mg + 4Cu at 190 °C (Fig. 2).

As concerning the tensile data, compared to AlSi10Mg alloy, higher YS and UTS values were also recorded for direct-aged AlSi10Mg + 4Cu samples (Fig. 8).

After direct aging, a large amount of Si and Cu precipitates are present and contribute to the overall strength of the heat-treated alloy. In AlSi10Mg + 4Cu sample aged at 190 °C for 2 h, Si and Cu precipitated to a large extent, thus reducing the solute amount in the matrix and, consequently, its contribution to the material strength. Furthermore, the precipitation of Si and θ-Al_2Cu particles broke the fine eutectic network (Fig. 7e,f,), limiting its contribution to the overall alloy strength. On the other hand, in AlSi10Mg + 4Cu sample aged ad 175 °C for 1 h, the precipitation strengthening is summed to the solid solution strengthening contribution since a not negligible solute amount is still present within the matrix. In addition, a fine eutectic network was also maintained after the heat-treatment (Fig. 7c), exploiting the grain boundary strengthening. This can be corroborated by the higher yield strength value (i.e., 325 MPa) achieved at 175 °C compared to its counterpart at 190 °C (i.e., 301 MPa).

From Fig. 8, it is also possible to observe that aged AlSi10Mg + 4Cu samples show lower YS and UTS values with respect to the corresponding as-built material. The origin for this discrepancy could be attributed to the presence of Cu inhomogeneities within the samples bulk (Fig. 1b). Indeed, the presence of such Cu segregations can speed-up the crack propagation during the tensile loading by cleavage, thus leading to an untimely failure. This fact can be corroborated by the brittle cleavage facets observed in Fig. 8c and the presence of several un-fused Cu particles found across the investigated fracture surfaces (Fig. A2). On the contrary, the 'embrittlement' effect induced by Cu segregations was not observed during hardness tests, being a static analysis.

The investigation conducted on the fracture surfaces of AlSi10Mg + 4Cu samples did not reveal significant differences between as-built and directly aged samples. Low-magnification surface topographies showed irregular cavities stemming from lack-of-fusion porosities and partially melted Cu particles (Fig. 9-a-b). This evidence suggested that the nucleation of the failure might have been in correspondence with such defects. Moreover, all samples exhibited fracture surfaces strewn of several holes with diameters of a size comparable to the laser scan track width (Fig. 9b) [23]. According to a theory proposed by Rosenthal et al. [50,51], these empty holes could have been originated from the detachment of laser scans aligned along the tensile direction.

Apart from the influence of laser scan tracks orientation, a ductile–brittle fracture was observed in AlSi10Mg + 4Cu samples (Fig. 9c). In these samples, the failure likely occurred via nucleation, growth and coalescence of several micro-voids located around nanometric precipitates (Fig. 9e), involving plastic deformation and yielding to the progressive formation of fine dimples (Fig. 9d). At the same time, the cleavage occurred in specific crystallographic directions, probably when the crack went through the un-melted Cu particles (Fig. A 2), as demonstrated from the presence of cleavage facets in Fig. 9c. Therefore, the higher the number of brittle particles, such as un-melted Cu or residual Si precipitates, encountered by the crack during propagation, the lower ductile was the tensile behavior of the alloy.

5. Conclusions

In this work, several strengthening strategies were applied to the AlSi10Mg alloy system. First, a high-strength AlSi10Mg + 4Cu alloy was successfully processed via *in-situ* alloying of elemental powders during LPBF to exploit both solid solution and precipitation strengthening mechanisms besides the fine microstructure typical of LPBF materials. In fact, the *in-situ* alloying yielded to a peculiar microstructure with a dual eutectic formed by Si precipitates intermixed with θ-Al_2Cu phase. A fraction of added Cu suddenly precipitated out during rapid cooling forming Al_2Cu precipitates while the Al lattice hosted the other fraction to form a super-saturated solid solution. Both contributions increased the micro-hardness of the base AlSi10Mg alloy by nearly 8.8 % and the YS value of 35.6 %.

Afterward, direct aging heat-treatment strategy was adopted to fully exploit the potential precipitation of Al_2Cu phase in AlSi10Mg + 4Cu samples. By heating the alloy at temperatures between 160 and 190 °C with a step of 15 °C, it was found that the age-hardening process was strictly dependent on the aging temperature. The higher was the aging temperature, the faster was the diffusion of Cu and Si solutes from super-saturated solid solution and, consequently, the nucleation of Si and θ-Al_2Cu secondary phases. By aging at 175 °C, the maximum hardness response was achieved after 1 h. In this condition, a mix of $\theta''/\theta' + \theta$ -Al_2Cu and Si phase suddenly precipitated, effectively strengthening the alloy. In this case, indeed, an increase of 25.3 % and 30 % for HV and YS, respectively, was attained with respect to AlSi10Mg alloy. A further increment of the aging temperature to 190 °C speeded-up the formation of the coherent and stable θ-Al_2Cu precipitates even if the fine eutectic network was broken, leading to a lower strengthening effect (HV, +18.9 %; YS, +20.4%).

It was then demonstrated that the direct aging heat treatment at 175 °C provided satisfying results in terms of hardness and yield strength increase with a limited heat-treatment time, i.e., 1 h. However, the applied direct aging heat treatments was not enough to dissolve Cu inhomogeneities formed within the sample bulk upon *in-situ* alloying, limiting the alloy ductility.

Data availability

The Authors declare that the main results supporting the findings of this work are available throughout this research article and in Appendix A.

CRediT authorship contribution statement

Federico Bosio: Conceptualization, Methodology, Validation, Investigation, Data curation, Writing – original draft, Writing – review & editing, Visualization. **Paolo Fino:** Supervision, Project administration, Funding acquisition. **Diego Manfredi:** Conceptualization, Writing – review & editing, Supervision. **Mariangela Lombardi:** Conceptualization, Writing – review & editing, Supervision, Project administration, Funding acquisition.

Declaration of Competing Interest

The authors declare that they have no known competing financial interests or personal relationships that could have appeared to influence the work reported in this paper.

Acknowledgements

The Authors would like to acknowledge the project "Joint research projects with top universities" of Politecnico di Torino and Compagnia di San Paolo. Dr. Alberta Aversa is greatly acknowledged for conducting EBSD analyses as a support of this research.

Appendix A

See Figs. A1-A3 and Table A1.

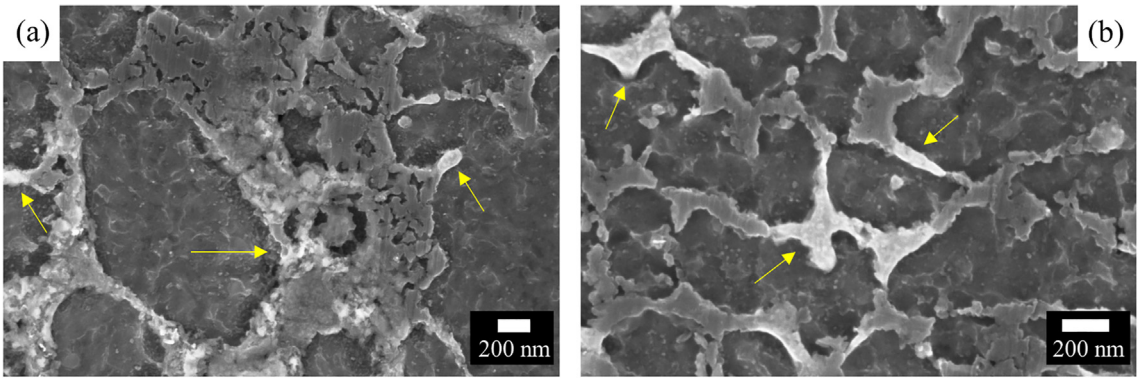

Fig. A1. FESEM micrographs of as-built AlSi10Mg + 4Cu samples at magnification of 100 k × using InLens detector. (a) A fine α-Al cell surrounded by Cu-rich areas intermixed with eutectic Si; (b) larger segments of eutectic enriched of Cu. Brighter regions corresponding to Cu-rich areas are pointed by yellow arrows.

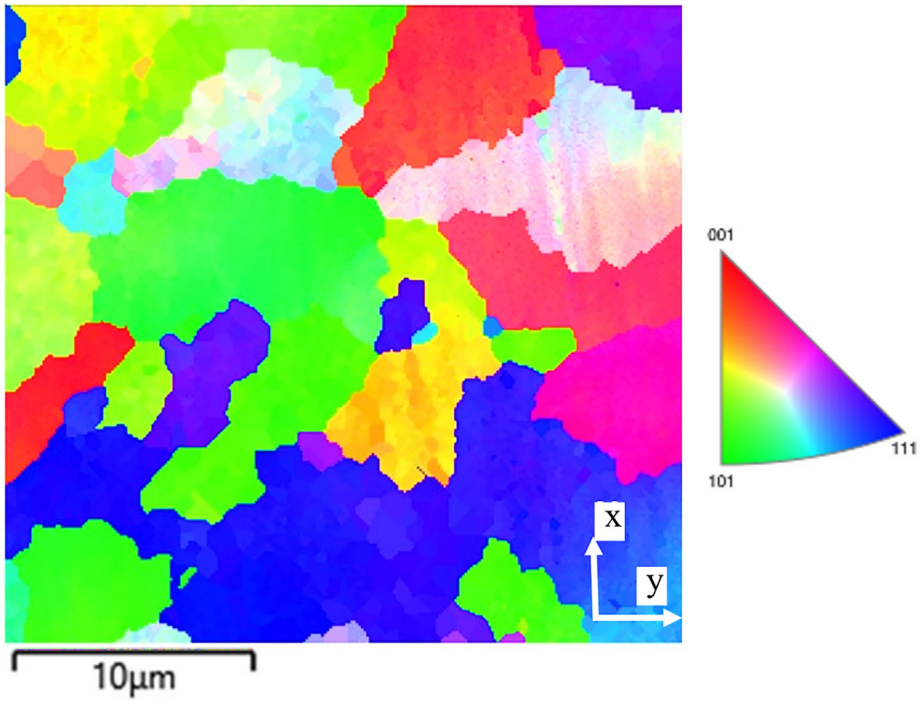

Fig. A2. EBSD maps of AlSi10Mg + 4Cu alloy revealing the Al grain structure on the XY plane (perpendicular to the building direction).

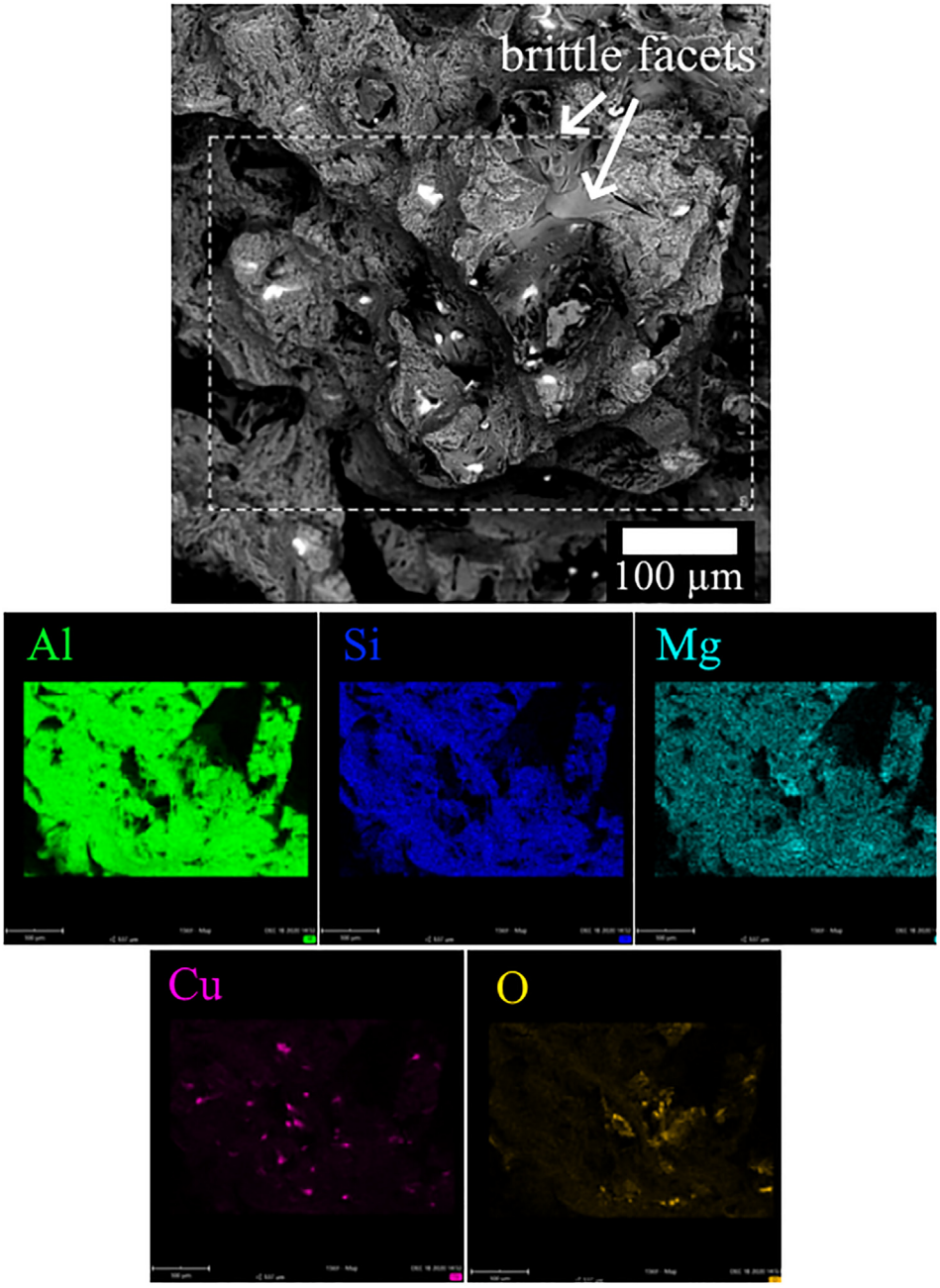

Fig. A3. Elemental compositional maps conducted on the fractured surface of AlSi10Mg + 4Cu alloy directly aged at 175 °C for 1 h.

Table A1
Results of the tensile tests conducted on as-built AlSi10Mg, as-built AlSi10Mg + 4Cu, and directly aged AlSi10Mg + 4Cu specimens.

Alloy	YS (MPa)		UTS (MPa)		ε (%)	
	Mean	St. Dev.	Mean	St. Dev.	Mean	St. Dev.
AlSi10Mg - AB	250	6.0	362	4.2	3.3	0.30
AlSi10Mg4Cu - AB	339	6.9	433	4.6	2.2	0.31
AlSi10Mg4Cu – 175 °C/1h	325	6.9	366	8.7	1.4	0.34
AlSi10Mg4Cu – 190 °C/2h	301	2.2	369	4.6	1.6	0.08

References

[1] N.T. Aboulkhair, M. Simonelli, L. Parry, I. Ashcroft, C. Tuck, R. Hague, 3D printing of aluminium alloys: additive manufacturing of aluminium alloys using selective laser melting, Prog. Mater. Sci. 106 (2019) 100578, https://doi.org/10.1016/j.pmatsci.2019.100578.

[2] T. DebRoy, H.L. Wei, J.S. Zuback, T. Mukherjee, J.W. Elmer, J.O. Milewski, A.M. Beese, A. Wilson-Heid, A. De, W. Zhang, Additive manufacturing of metallic components – process, structure and properties, Prog. Mater. Sci. 92 (2018) 112–224, https://doi.org/10.1016/j.pmatsci.2017.10.001.

[3] S.A.M. Tofail, E.P. Koumoulos, A. Bandyopadhyay, S. Bose, L. O'Donoghue, C. Charitidis, Additive manufacturing: scientific and technological challenges, market uptake and opportunities, Mater. Today. 21 (1) (2018) 22–37, https://doi.org/10.1016/j.mattod.2017.07.001.

[4] I. Yadroitsev, P. Krakhmalev, I. Yadroitsava, Titanium alloys manufactured by in situ alloying during laser powder bed fusion, Jom. 69 (12) (2017) 2725–2730, https://doi.org/10.1007/s11837-017-2600-7.

[5] P. Yuan, D. Gu, Molten pool behaviour and its physical mechanism during selective laser melting of TiC/AlSi10Mg nanocomposites: Simulation and experiments, J. Phys. D. Appl. Phys. 48 (3) (2015) 035303, https://doi.org/10.1088/0022-3727/48/3/035303.

[6] V. Semak, A. Matsunawa, The role of recoil pressure in energy balance during laser materials processing, J. Phys. D. Appl. Phys. 30 (18) (1997) 2541–2552, https://doi.org/10.1088/0022-3727/30/18/008.

[7] P. Wang, K.G. Prashanth, S. Pauly, J. Eckert, S. Scudino, Microstructure and mechanical properties of Al-Cu alloys fabricated by selective laser melting of powder mixtures, 735 (2018) 2263–2266. https://doi.org/10.1016/j.jallcom.2017.10.168.

[8] M.L. Montero-Sistiaga, R. Mertens, B. Vrancken, X. Wang, B. Van Hooreweder, J.-P. Kruth, J. Van Humbeeck, Van Humbeeck, Changing the alloy composition of Al7075 for better processability by selective laser melting, Elsevier B.V. 238 (2016) 437–445, https://doi.org/10.1016/j.jmatprotec.2016.08.003.

[9] R. Casati, M. Coduri, M. Riccio, A. Rizzi, M. Vedani, Development of a high strength Al-Zn-Si-Mg-Cu alloy for selective laser melting, J. Alloy. Compd. Submitt. 801 (2019) 243–253, https://doi.org/10.1016/j.jallcom.2019.06.123.

[10] P. Vora, R. Martinez, N. Hopkinson, I. Todd, K. Mumtaz, Customised alloy blends for in-situ Al339 alloy formation using anchorless selective laser melting, Technologies. 5 (2017) 24, https://doi.org/10.3390/technologies5020024.

[11] G. Cattano, Feasibility studies on laser powder bed fusion of powders mixtures based on aluminium alloys or high entropy alloys, Politecnico di Torino (2019). https://core.ac.uk/download/pdf/234930686.pdf.

[12] D. Gianoglio, S. Marola, L. Battezzati, A. Aversa, F. Bosio, M. Lombardi, D. Manfredi, M. Lorusso, Banded microstructures in rapidly solidified Al-3 wt% Er, Intermetallics 119 (2020) 106724, https://doi.org/10.1016/j.intermet.2020.106724.

[13] I.J. Polmear, Novel materials and processing methods, in: Light Alloy. From Tradit. Alloy. to Nanocrystals, Elsevier, 2006: pp. 367–412.

[14] I.J. Polmear, Physical metallurgy of aluminium alloys, in: Light Alloy. From Tradit. Alloy. to Nanocrystals, Elsevier, 2006: pp. 29–96.

[15] J. Silcock, T. Heal, H. Hardy, Structural ageing characteristics of aluminum-copper alloys, J. Inst. Met. 82 (n.d.) 239–248.

[16] ASTM International B917/B917M-12, Standard practice for heat treatment of aluminum-alloy castings from all processes, ASTM B. Stand. 01 (2012) 1–11, https://doi.org/10.1520/B0917.

[17] D.A. Porter, K.E. Easterling, Diffusional Transformations in Solids, in: Springer science (Ed.), Phase Transform. Met. Alloy., 1992: pp. 291–308. https://doi.org/10.1007/978-1-4899-3051-4.

[18] M. Coduri, M. Hamidi Nasab, M. Vedani, R. Casati, V. Tirelli, Effects of platform pre-heating and thermal-treatment strategies on properties of AlSi10Mg alloy processed by selective laser melting, Metals (Basel) 8 (2018) 954, https://doi.org/10.3390/met8110954.

[19] C.H.J. Davies, K. Zhang, J.H. Rao, X. Wu, A. Huang, Y. Zhang, Multiple precipitation pathways in an Al-7Si-0.6Mg alloy fabricated by selective laser melting, Scr. Mater. 160 (2018) 66–69, https://doi.org/10.1016/j.scriptamat.2018.09.045.

[20] F. Bosio, H. Shen, Y. Liu, M. Lombardi, P. Rometsch, X. Wu, Y. Zhu, A. Huang, Production strategy for manufacturing large-scale AlSi10Mg components by laser powder bed fusion, Jom. 73 (3) (2021) 770–780, https://doi.org/10.1007/s11837-020-04523-8.

[21] N.T. Aboulkhair, C. Tuck, I. Ashcroft, I. Maskery, N.M. Everitt, On the precipitation hardening of selective laser melted AlSi10Mg, Metall. Mater. Trans. A. 46 (8) (2015) 3337–3341, https://doi.org/10.1007/s11661-015-2980-7.

[22] M. Roudnická, O. Molnárová, D. Dvorský, L. Křivský, D. Vojtěch, Specific response of additively manufactured AlSi9Cu3Fe alloy to precipitation strengthening, Met. Mater. Int. 26 (8) (2020) 1168–1181, https://doi.org/10.1007/s12540-019-00504-y.

[23] F. Bosio, A. Aversa, M. Lorusso, S. Marola, D. Gianoglio, L. Battezzati, P. Fino, D. Manfredi, M. Lombardi, A time-saving and cost-effective method to process alloys by laser powder bed fusion, Mater. Des. 181 (2019) 107949, https://doi.org/10.1016/j.matdes.2019.107949.

[24] S. Marola, D. Gianoglio, F. Bosio, A. Aversa, M. Lorusso, D. Manfredi, M. Lombardi, L. Battezzati, Alloying AlSi10Mg and Cu powders in laser Single Scan Tracks, melt spinning, and Laser Powder Bed Fusion, J. Alloys Compd. 821 (2020) 153538, https://doi.org/10.1016/j.jallcom.2019.153538.

[25] H.A. Ferguson, Heat treating of aluminium alloy, Heat Treat. Alum. Alloy. 4 (1991) 841–879, https://doi.org/10.1361/asmhba0001205.

[26] D. Manfredi, F. Calignano, M. Krishnan, R. Canali, E.P. Ambrosio, E. Atzeni, From powders to dense metal parts: characterization of a commercial alsimg alloy processed through direct metal laser sintering, Materials (Basel). 6 (2013) 856–869, https://doi.org/10.3390/ma6030856.

[27] L. Thijs, K. Kempen, J.-P. Kruth, J. Van Humbeeck, Fine-structured aluminium products with controllable texture by selective laser melting of pre-alloyed AlSi10Mg powder, Acta Mater. 61 (5) (2013) 1809–1819, https://doi.org/10.1016/j.actamat.2012.11.052.

[28] H. Rao, S. Giet, K. Yang, X. Wu, C.H.J. Davies, The influence of processing parameters on aluminium alloy A357 manufactured by Selective Laser Melting, Mater. Des. 109 (2016) 334–346, https://doi.org/10.1016/j.matdes.2016.07.009.

[29] H.B. Dong, P.D. Lee, Simulation of the columnar-to-equiaxed transition in directionally solidified Al-Cu alloys, Acta Mater. 53 (3) (2005) 659–668, https://doi.org/10.1016/j.actamat.2004.10.019.

[30] P. Van Cauwenbergh, V. Samaee, L. Thijs, J. Nejezchlebová, P. Sedlák, A. Iveković, Unravelling the multi - scale structure – property relationship of laser powder bed fusion processed and heat - treated, Sci. Rep. (2021) 1–15, https://doi.org/10.1038/s41598-021-85047-2.

[31] S. Marola, D. Manfredi, G. Fiore, M.G. Poletti, M. Lombardi, P. Fino, L. Battezzati, A comparison of Selective Laser Melting with bulk rapid solidification of AlSi10Mg alloy, J. Alloys Compd. 742 (2018) 271–279, https://doi.org/10.1016/j.jallcom.2018.01.309.

[32] G. Riontino, A. Zanada, Coupled formation of hardening particles on pre-precipitates in an Al-Cu-Mg-Si 2014 alloy, Mater. Lett. 37 (1998) 241–245. https://doi.org/10.1016/S0167-577X(98)00099-8.

[33] Riccardo Casati, Maurizio Vedani, Aging Response of an A357 Al Alloy Processed by Selective Laser Melting, Adv. Eng. Mater. 21 (4) (2019) 1800406, https://doi.org/10.1002/adem.201800406.

[34] J. Fiocchi, A. Tuissi, P. Bassani, C.A. Biffi, Low temperature annealing dedicated to AlSi10Mg selective laser melting products, J. Alloys Compd. 695 (2017) 3402–3409, https://doi.org/10.1016/j.jallcom.2016.12.019.

[35] R. Casati, M. Coduri, S. Checchia, M. Vedani, Insight into the effect of different thermal treatment routes on the microstructure of AlSi7Mg produced by laser powder bed fusion, Mater. Charact. 172 (2021) 110881, https://doi.org/10.1016/j.matchar.2021.110881.

[36] S.C. Wang, M.J. Starink, Precipitates and intermetallic phases in precipitation hardening Al-Cu-Mg-(Li) based alloys, Int. Mater. Rev. 50 (4) (2005) 193–215, https://doi.org/10.1179/174328005X14357.

[37] P. Ma, K. Prashanth, S. Scudino, Y. Jia, H. Wang, C. Zou, Z. Wei, J. Eckert, Influence of annealing on mechanical properties of Al-20Si processed by selective laser melting, Metals (Basel). 4 (2014) 28–36, https://doi.org/10.3390/met4010028.

[38] K.G. Prashanth, S. Scudino, J. Eckert, Defining the tensile properties of Al-12Si parts produced by selective laser melting, Acta Mater. 126 (2017) 25–35, https://doi.org/10.1016/j.actamat.2016.12.044.

[39] K.G. Prashanth, S. Scudino, H.J. Klauss, K.B. Surreddi, L. Löber, Z. Wang, A.K. Chaubey, U. Kühn, J. Eckert, Microstructure and mechanical properties of Al-12Si produced by selective laser melting: Effect of heat treatment, Mater. Sci. Eng. A. 590 (2014) 153–160, https://doi.org/10.1016/j.msea.2013.10.023.

[40] X.P. Li, X.J. Wang, M. Saunders, A. Suvorova, L.C. Zhang, Y.J. Liu, M.H. Fang, Z.H. Huang, T.B. Sercombe, A selective laser melting and solution heat treatment refined Al-12Si alloy with a controllable ultrafine eutectic microstructure and 25% tensile ductility, Acta Mater. 95 (2015) 74–82, https://doi.org/10.1016/j.actamat.2015.05.017.

[41] P. Rometsch, Q. Jia, K. V. Yang, X. Wu, Aluminum alloys for selective laser melting – towards improved performance, Elsevier Inc., 2019. https://doi.org/10.1016/b978-0-12-814062-8.00016-9.

[42] K.V. Yang, P. Rometsch, C.H.J. Davies, A. Huang, X. Wu, Effect of heat treatment on the microstructure and anisotropy in mechanical properties of A357 alloy produced by selective laser melting, Mater. Des. 154 (2018) 275–290, https://doi.org/10.1016/j.matdes.2018.05.026.

[43] S. Kou, Basic Solidification Concepts, in: Weld. Metall., John Wiley & Sons, 2003: pp. 145–169.

[44] S. Kou, Weld Metal Solidification I: Grain Structure, in: Weld. Metall., John Wiley & Sons, 2003: pp. 170–198.

[45] S. Marola, S. Bosia, A. Veltro, G. Fiore, D. Manfredi, M. Lombardi, G. Amato, M. Baricco, L. Battezzati, Residual stresses in additively manufactured AlSi10Mg: Raman spectroscopy and X-ray diffraction analysis, Mater. Des. 202 (2021) 109550. https://doi.org/10.1016/j.matdes.2021.109550.

[46] M.J. Starink, L.F. Cao, P.A. Rometsch, A model for the thermodynamics of and strengthening due to co-clusters in Al-Mg-Si-based alloys, Acta Mater. 60 (10) (2012) 4194–4207, https://doi.org/10.1016/j.actamat.2012.04.032.

[47] Jeremy H. Rao, Yong Zhang, Kai Zhang, Xinhua Wu, Aijun Huang, Selective laser melted Al-7Si-0.6Mg alloy with in-situ precipitation via platform heating for residual strain removal, Mater. Des. 182 (2019) 108005, https://doi.org/10.1016/j.matdes.2019.108005.

[48] O.R. Myhr, O. Grong, S.J. Andersen, Modelling of the age hardening behaviour of Al-Mg-Si alloys, Acta Mater. 49 (2001) 65–75, https://doi.org/10.1016/S1359-6454(00)00301-3.

[49] J.D. EMBURY, D.J. LLOYD, T.R. RAMACHANDRAN, Strengthening Mechanisms in Aluminum Alloys, 31 (1989) 579–601. https://doi.org/10.1016/b978-0-12-341831-9.50027-9.
[50] I. Rosenthal, A. Stern, N. Frage, Strain rate sensitivity and fracture mechanism of AlSi10Mg parts produced by selective laser melting, Mater. Sci. Eng. A. 682 (2017) 509–517, https://doi.org/10.1016/j.msea.2016.11.070.
[51] I. Rosenthal, R. Shneck, A. Stern, Heat treatment effect on the mechanical properties and fracture mechanism in AlSi10Mg fabricated by additive manufacturing selective laser melting process, Mater. Sci. Eng. A. 729 (2018) 310–322, https://doi.org/10.1016/j.msea.2018.05.074.